HAL
open science

Interplay of inequivalent atomic positions in resonant x-ray diffraction of Fe3BO6

Guillaume Beutier, E.N. Ovchinnikova, S. P. Collins, Vladimir-E. Dmitrienko, José-Emilio Lorenzo, Jean-Louis Hodeau, A. Kirfel, Yves Joly, A. A. Antonenko, V. A. Sarkisyan, et al.

To cite this version:

Guillaume Beutier, E.N. Ovchinnikova, S. P. Collins, Vladimir-E. Dmitrienko, José-Emilio Lorenzo, et al.. Interplay of inequivalent atomic positions in resonant x-ray diffraction of Fe3BO6. Journal of Physics: Condensed Matter, 2009, 21, pp.265402. 10.1088/0953-8984/21/26/265402 . hal-00687306

HAL Id: hal-00687306

https://hal.science/hal-00687306v1

Submitted on 12 Apr 2012

HAL is a multi-disciplinary open access archive for the deposit and dissemination of scientific research documents, whether they are published or not. The documents may come from teaching and research institutions in France or abroad, or from public or private research centers.

L'archive ouverte pluridisciplinaire **HAL**, est destinée au dépôt et à la diffusion de documents scientifiques de niveau recherche, publiés ou non, émanant des établissements d'enseignement et de recherche français ou étrangers, des laboratoires publics ou privés.

IOP PUBLISHING JOURNAL OF PHYSICS: CONDENSED MATTER

J. Phys.: Condens. Matter **21** (2009) 265402 (12pp) doi:10.1088/0953-8984/21/26/265402

Interplay of inequivalent atomic positions in resonant x-ray diffraction of Fe_3BO_6

G Beutier[1], E Ovchinnikova[2], S P Collins[1], V E Dmitrienko[3], J E Lorenzo[4], J-L Hodeau[4], A Kirfel[5], Y Joly[4], A A Antonenko[2], V A Sarkisyan[3,6] and A Bombardi[1]

[1] Diamond Light Source, Harwell Science and Innovation Campus, OX11 0DE, UK
[2] Department of Physics of Moscow State University, 119899 Moscow, Russia
[3] AV Shubnikov Institute of Crystallography, 119333, Moscow, Russia
[4] Institut Louis Néel, CNRS, BP 166X, F-38042 Grenoble, France
[5] Steinmann Institute, University of Bonn, Poppelsdorfer Schloss, D-53115 Bonn, Germany

E-mail: guillaume.beutier@diamond.ac.uk

Received 19 February 2009, in final form 20 May 2009
Published 11 June 2009
Online at stacks.iop.org/JPhysCM/21/265402

Abstract
'Forbidden' Bragg reflections of iron orthoborate Fe_3BO_6 were studied theoretically and experimentally in the vicinity of the iron K edge. Their energy spectra are explained as resulting from the interference of x-rays scattered from two inequivalent crystallographic sites occupied by iron ions. This particular structure property gives rise to complex azimuthal dependences of the reflection intensities in the pre-edge region as they result from the interplay of site specific dipole–quadrupole and quadrupole–quadrupole resonant scattering. Also evidenced is an anisotropic character of the absorption spectrum. Self-absorption correction to the diffraction data, as well as possible contributions of thermal vibrations and magnetic order, are discussed. Particular care is given to extracting clean spectra from the data, and it is demonstrated that excellent results can be obtained even from measurements that appear corrupted by several effects such as poor crystal quality and multiple scattering.

(Some figures in this article are in colour only in the electronic version)

1. Introduction

Resonant x-ray scattering (RXS) has emerged in the last two decades as a popular method for studying local properties of crystals, such as magnetic, charge and orbital ordering, thermal vibrations etc [1–4]. The anisotropy of the tensor of scattering in the vicinity of an absorption edge allows for the observation of Bragg reflections that are forbidden in the isotropic case by glide-plane and/or screw-axis symmetries. Such reflections were first observed by Templeton and Templeton [5] and theoretically described in [6, 7]. Since then, 'forbidden' reflections were studied experimentally in many crystals. They are also referred to as pure resonant reflections, because they appear only very close to absorption edges owing to resonant scattering processes. Because of this energy constraint and of their weakness, they can be measured only with synchrotron radiation.

The sensitivity of RXS to local anisotropy arises from multipole electronic transitions and is hence described in terms of scattering tensors of various ranks. The strongest contributions to pure resonant reflections are provided by the so called dipole–dipole scattering. Beyond this, there are numerous physical phenomena contributing to the resonant reflections. Higher order contributions, like dipole–quadrupole [8–10] or quadruple–quadrupole [11, 12], become important when the dipole–dipole contribution vanishes because of symmetry restrictions or physical selection rules. In magnetic crystals, the magnetic reflections are mainly provided by the antisymmetric part of the dipole–dipole contribution [13–15]. The co-existence of both a magnetic structure and local crystal anisotropy can, in principle, give rise to so-called 'combined' forbidden reflections [16], which have not been observed so far. The study of RXS in GdB_4 in [17] revealed both time-even and time-odd (magnetic) dipole–dipole contributions to forbidden reflections dominating at different temperatures. The situation becomes even more

[6] Present address: Beam Engineering for Advanced Measurements Corporated, 809 South Orlando Avenue, Suite I, Winter Park, FL 32789, USA.

 © 2009 IOP Publishing Ltd Printed in the UK

complicated by the possibility of further effects contributing to forbidden reflections. Contributions associated with thermal vibrations and point defects were predicted in [18, 19], and thermal-motion-induced (TMI) reflections were observed in Ge [20–22], ZnO [23] and GaN [24]. In addition, there can be non-resonant scattering arising from magnetic modulations. The interference between non-resonant magnetic scattering and resonant dipole–quadrupole and quadrupole–quadrupole channels was found in hematite (α-Fe_2O_3) [25]. Thus, in many cases, the energy spectra of forbidden reflections can be explained as the result of the interference between two or more scattering channels, revealing in this way an interesting physics of electronic interactions. Interference phenomena may be even more important when the resonant atoms occupy different crystallographic sites. Such a situation was observed in magnetite Fe_3O_4 [26]. There, the 16(b) position of iron provides the $h00, h = 4n + 2$ reflections corresponding to the dipole–dipole scattering with a maximum close to the absorption edge, while the ions in the 8(a) positions allow only for an essential dipole–quadrupole term in the pre-edge. Thus the peaks corresponding to the different positions are separated in energy. For garnets, it was shown that different atomic positions can provide different forbidden reflections [27].

So far, in all studied cases the interference between various scattering processes or different atomic positions could be disentangled by taking advantage of their manifestation at different energies or thanks to crystallographic selection rules. Here we report the case of iron orthoborate (Fe_3BO_6), in which scattering from two inequivalent crystallographic positions interferes, and this following the same selection rules and featuring the same tensor components. Using theoretical analysis and careful data treatment, we demonstrate that RXS is now a technique sufficiently mature to study such a complicated case, even in the presence of experimental complications such as poor crystal quality, self-absorption and multiple scattering.

2. Theoretical

In kinematic diffraction theory, which is usually applied to RXS, a forbidden reflection intensity is simply determined by the resonant structure amplitude $F(\boldsymbol{H})$, defined by the resonant scatterer's position and by the Fourier transform of the atomic scattering factor $f(\boldsymbol{r})$. The latter can be decomposed into

$$f = f^0 + \mathrm{i} f^{\mathrm{m}} + f' + \mathrm{i} f'' \tag{1}$$

where f^0 is the energy independent non-resonant charge scattering factor and f^{m} accounts for non-resonant magnetic scattering. The last two energy dependent terms describe the real and imaginary parts of the RXS and obtain particular importance at energies close to an absorption edge.

The tensor character and the tensorial properties of atomic scattering factors near absorption edges were considered in many studies both in a Cartesian approach [28, 29] and also using spherical tensors [14, 12, 30, 31]. In the present paper we shall use the Cartesian formalism. Within this framework, the resonant scattering can be written in the form of a superposition of the interactions in different multipole orders,

$$f' + \mathrm{i} f'' = e_j'^{*} e_k \left[D_{jk} - \frac{\mathrm{i}}{2}(k_m I_{jkm} - k_m' I_{kjm}^{*}) + \frac{1}{4} k_m' k_n Q_{jkmn} \right] \tag{2}$$

where the summation over repeated indices is implied.

The vectors $\boldsymbol{k}$, $\boldsymbol{k}'$ and $\boldsymbol{e}$, $\boldsymbol{e}'$ are the wavevectors and polarizations, respectively, of the incident and scattered radiations. Below we shall also use conventional $\boldsymbol{\sigma}$ and $\boldsymbol{\pi}$ polarization vectors, normal and parallel, respectively, to the scattering plane. The multipolar expansion was extended up to the electric quadrupolar term, omitting magnetic multipolar and higher order electric multipolar contributions, which can be expected to be extremely weak [30]. Thus, the resonant scattering tensor consists only of the second rank dipole–dipole tensor $\boldsymbol{D}$, the third rank dipole–quadrupole tensor $\boldsymbol{I}$, and the fourth rank quadrupole–quadrupole tensor $\boldsymbol{Q}$, all of which possess tensor elements that are sensitive to the incident radiation energy.

The symmetry properties of these tensors, in the Cartesian formalism, are the following. (i) The dipole–dipole tensor is symmetric ($D_{jk} = D_{kj}$) for non-magnetic crystals. For magnetic crystals, the magnetic character manifests itself as an antisymmetric part. (ii) The time-even dipole–quadrupole tensor can have both a symmetric and an antisymmetric part with respect to permutation of the polarization indices. It was shown that the symmetric part of the time-even dipole–quadrupole tensor gives rise to forbidden reflections in Ge and ZnO [8, 20, 21, 23], whereas the antisymmetric part causes some peculiarities of the forbidden reflections in Fe_2O_3 and Cr_2O_3 [9, 10, 25]. A time-odd third rank tensor can also occur in the case of a magnetic crystal. (iii) In non-magnetic crystals, the fourth rank quadrupole–quadrupole tensor is symmetric, i.e. invariant against the permutation of polarization or wavevector indices [28]: $Q_{jknm} = Q_{kjnm} = Q_{jkmn} = Q_{kjmn} = Q_{nmjk}$. These symmetry properties reduce the numbers of 'distinct' Cartesian components, for a non-magnetic crystal, to 6, 15 and 21 for the dipole–dipole, dipole–quadrupole, and quadrupole–quadrupole tensors, respectively [32]. However, spherical formalism shows that the numbers of independent components are 6, 15 and 15 respectively. The remaining distinct Cartesian components are therefore linearly related, although their linear relationship is not trivial [33].

Generally, the intensity of a forbidden reflection is dominated by the dipole–dipole contribution. However, when this contribution vanishes, e.g. due to crystal symmetry, the higher order terms become the essential ones. They are also important in the pre-edge region, where the dipole–dipole contribution is weak: quadrupole transitions are reduced in energy due to multi-electron effects such as screening.

Since the tensorial character of the resonant scattering factor causes the reflection intensities to obtain azimuthal dependences, it is essential to identify the non-vanishing tensor elements in order to understand the azimuthal properties of forbidden reflections and their energy dependences. Exactly this analytical task is completed in the following section for the title compound, Fe_3BO_6.

3. Pure resonant reflections in iron orthoborate

The symmetry of iron orthoborate structure is described by the space group $Pnma$ (no 62) [34]. The Fe cations occupy two octahedral positions: a special one, 4(c), with point symmetry m (the mirror plane m is normal to [010]), and a general one, 8(d), with point symmetry 1 (i.e. no symmetry restrictions). The resonant structure factor $F(\boldsymbol{H})$ thus sums the contributions of the four and eight, respectively, Fe cations of both groups:

$$F(\boldsymbol{H}) = F^{4(c)}(\boldsymbol{H}) + F^{8(d)}(\boldsymbol{H}). \tag{3}$$

Naturally, the ratio between the partial structure factors, $F^{4(c)}$ and $F^{8(d)}$, varies when the scattering factors vary with the reflection indices. Moreover, their relative phases vary strongly upon crossing an absorption edge. Below, it will be shown that the complex interplay between the scattering at the two Fe positions can produce constructive or destructive interference, leading to completely different energy spectra for different $\boldsymbol{H} = hkl$.

The pure resonant reflections discussed in the present paper are similar to the pure nuclear reflections of Mössbauer radiation, but the energy spectra are quite different. In the case of nuclear scattering the resonant peaks are very sharp ($\sim 10^{-8}$ eV), while for electronic transitions the typical width of resonance lines is about 1–10 eV. Iron orthoborate has indeed been extensively studied with Mössbauer radiation, and the interplay between the two iron positions was evidenced [35, 36]. Because the Mössbauer nuclear transition in iron is very sensitive to magnetism, it allows for the determination of the magnetic structure of iron orthoborate [37, 38]. In the case of RXS, we are dealing with K-edge electronic transitions of the $E1$ and $E2$ types, which are only weakly sensitive to magnetism. We will therefore develop our tensor analysis treating Fe as non-magnetic. The validity of this approximation will be demonstrated by the experiment.

Next, we determine the contributions to the resonant structure factor, being allowed by space group symmetry. We shall first analyse the case of the general position 8(d), with general coordinates (x, y, z) in the unit cell, and then proceed to the special position 4(c), which second case can be easily deduced from the first one. In a general position (i.e. point symmetry 1), the symmetric D, I and Q tensors can have up to 6, 18 and 21, respectively, distinct Cartesian components [32], some of which vanish for particular hkl values. In the case of $h00, h = 2n + 1$, reflections, which are the experimentally measured reflections, only one, D_{xz}, of the six Cartesian components of the dipole–dipole tensor survives and gives rise to the following contribution to the structure factor, where the fractional coordinates (x, y, z) refer to the crystal axes (figure 1):

$$F_{dd}(h = 2n+1, 0, 0) = 8D_{xz}\cos(2\pi hx)\begin{pmatrix} 0 & 0 & 1 \\ 0 & 0 & 0 \\ 1 & 0 & 0 \end{pmatrix}. \tag{4}$$

Similarly, the dipole–quadrupole tensor has a structure factor with only five non-vanishing distinct Cartesian components at the $h00, h = 2n+1$, forbidden reflections: I_{xxz}, I_{yyz}, I_{zxx}, I_{zyy} and I_{zzz}. Describing $\boldsymbol{k}$ and $\boldsymbol{k}'$ with respect to the crystal (x, y, z) coordinate system (figure 1), we obtain

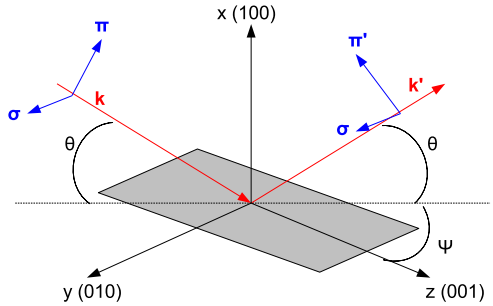

Figure 1. Diagram of the experimental geometry and definition of the coordinate system. In this Cartesian system (x, y, z), the vectors $\boldsymbol{k}, \boldsymbol{k}', \boldsymbol{\sigma}, \boldsymbol{\pi}$ and $\boldsymbol{\pi}'$ are written as follows:
$\boldsymbol{k} = |k|(-\sin\theta, -\cos\theta\sin\psi, \cos\theta\cos\psi)$;
$\boldsymbol{k}' = |k|(\sin\theta, -\cos\theta\sin\psi, \cos\theta\cos\psi)$; $\boldsymbol{\sigma} = (0, \cos\psi, \sin\psi)$;
$\boldsymbol{\pi} = (\cos\theta, -\sin\theta\sin\psi, \sin\theta\cos\psi)$;
$\boldsymbol{\pi}' = (\cos\theta, \sin\theta\sin\psi, -\sin\theta\cos\psi)$.

$$F_{dq}(h = 2n+1, 0, 0) = 4|\boldsymbol{k}|\sin(2\pi hx)\begin{pmatrix} 0 & 0 & \tilde{I}_{xz} \\ 0 & 0 & -\tilde{I}_{yz} \\ \tilde{I}_{xz} & \tilde{I}_{yz} & 0 \end{pmatrix} \tag{5}$$

with

$$\tilde{I}_{xz} = -(I_{xxz} + I_{zxx})\sin\theta \tag{6}$$

$$\tilde{I}_{yz} = (I_{yyz} - I_{zyy})\cos\theta\sin\psi. \tag{7}$$

The term I_{zzz} vanishes because $k_z = k'_z$. For the dipole–quadrupole contribution we see that there are both a symmetric and an antisymmetric part.

Finally, one finds that only 4 of the 21 distinct Cartesian components of the quadrupole–quadrupole tensor contribute to the $h00, h = 2n + 1$, reflections:

$$F_{qq}(h = 2n+1, 0, 0) = 2|\boldsymbol{k}|^2\cos(2\pi hx) \times \begin{pmatrix} 0 & \tilde{Q}_{xy} & \tilde{Q}_{xz} \\ \tilde{Q}_{xy} & 0 & 0 \\ \tilde{Q}_{xz} & 0 & 0 \end{pmatrix} \tag{8}$$

with

$$\tilde{Q}_{xy} = -Q_{xyyz}\cos^2\theta\sin 2\psi \tag{9}$$

$$\tilde{Q}_{xz} = -Q_{xxxz}\sin^2\theta + \cos^2\theta(Q_{xzyy}\sin^2\psi + Q_{xzzz}\cos^2\psi). \tag{10}$$

By substituting the polarizations $\sigma = \sigma'$, π and π' by their Cartesian expressions in equations (4), (5) and (8), we conclude that the x-rays are scattered only in the rotated channels, i.e. $\sigma \to \pi$ and $\pi \to \sigma$. For the former one, which is the case of the experimental set-up, we obtain the following contributions:

$$F^{\sigma\pi}_{dd}(h = 2n+1, 0, 0) = 8D_{xz}\cos(2\pi hx)\cos\theta\sin\psi \tag{11}$$

$$F^{\sigma\pi}_{dq}(h = 2n+1, 0, 0) = -2|\boldsymbol{k}|(I_{yyz} - I_{zyy} - I_{xxz} - I_{zxx}) \times \sin(2\pi hx)\sin 2\theta\sin\psi \tag{12}$$

$$F^{\sigma\pi}_{qq}(h = 2n+1, 0, 0) = 2|\boldsymbol{k}|^2\cos(2\pi hx) \times [Q_1(\theta)\sin\psi + Q_3(\theta)\sin 3\psi] \tag{13}$$

Table 1. Weights to the contributions in the $h00$, $h = 2n + 1$, forbidden reflections of the two sites with positions $x_d = 0.128\,35$ and $x_c = 0.412\,46$. Positions from [39].

(h, k, l)	$\cos(2\pi h x_c)$	$\sin(2\pi h x_c)$	$\cos(2\pi h x_d)$	$\sin(2\pi h x_d)$
300	0.079	0.997	−0.750	0.661
500	0.924	0.381	−0.628	−0.777
700	0.7591	−0.650	0.803	−0.595

where $Q_1(\theta)$ and $Q_3(\theta)$ are linear combinations of Q_{xxxz}, Q_{xyyz}, Q_{xzzz} and Q_{xzyy} with coefficients depending on θ only. This analysis shows that the dipole–dipole and dipole–quadrupole amplitudes of the scattered radiation possess a simple $\sin\psi$ azimuthal dependence, while the quadrupole–quadrupole contribution mixes $\sin\psi$ and $\sin 3\psi$ terms.

The above expressions were derived in the case of the general 8(d) position, for which no symmetry applies to the atomic site. We end up with six contributions to the forbidden reflections $h00$, $h = 2n + 1$: one for the dipole–dipole (D_{xz}), one for the dipole–quadrupole (a fixed combination of the I_{jkn}), and four for the quadrupole–quadrupole. Let us now analyse the case of ions in 4(c) positions with point symmetry m: they lie on the mirror planes ($y = \frac{1}{4}$ and equivalent planes) which transform (xyz) into $(x, \frac{1}{2} - y, z)$, etc. Thus, all the Cartesian tensor components with indices containing odd powers of y vanish. However, equations (11)–(13) do not involve such components for the $h00$, $h = 2n + 1$, reflections so that the scattering description for the cations in the 4(c) positions needs as many components as do the cations in general 8(d) positions. Consequently, for reflections $h00$, $h = 2n + 1$, the resonant amplitude scattered by each iron site is described by six parameters, i.e. 12 in total, all of which vary with energy. In principle, it would be possible to determine them all, by measuring all six $h00$, $h = 2n + 1$, forbidden reflections accessible at the iron K-edge energy, at two different azimuths. But it would be extremely tedious, if experimentally possible, and it is not the purpose of the present article. Here we want to highlight the interference between non-equivalent crystallographic sites.

The scattering contributions interfere with weights $\cos(2\pi hx)$ for the dipole–dipole and quadrupole–quadrupole, and $\sin(2\pi hx)$ for the dipole–quadrupole, respectively, where $x = x_d = 0.412\,46$ for the iron in the 8(d) and $x = x_c = 0.128\,35$ for the other iron in the 4(c) position [39]. The values of the respective coefficients are given in table 1. Inspecting these values we can see that the dipole–dipole contribution to the 300 reflection is mainly provided by Fe in 8(d). We can further see that the dipole–dipole contributions from 8(d) and 4(c) to the 300 and 500 reflections have opposite signs while those to reflection 700 show comparable values and equal signs. Thus, the interference between the radiation scattered by the two iron sites is of the same type for the reflections 300 and 500, and opposite for the 700 reflection, so that significant differences between the energy spectra of the 300, 500 and 700 reflections can be expected.

4. Experimental details

The resonant reflections 300, 500 and 700 were measured at the XMaS beamline of the European Synchrotron Radiation Facility (ESRF) at room temperature. Complementary measurements of the fluorescence yield and of the resonant reflection 700 at ambient as well as at low and high temperatures were done at beamline I16 of the Diamond Light Source (DLS). The natural linear polarization of the radiation obtained at the bending magnet (XMaS) or undulator (I16) was used and the energy was tuned to the Fe K edge with a Si(111) monochromator. At both beamlines, the scattered radiation was measured with silicon-drift detectors, allowing simultaneous records of the elastic scattering and the fluorescence yield in independent channels. Since, as shown above, the resonant scattering involves a full $\sigma \rightarrow \pi$ polarization change, it was not necessary to use a secondary polarization analyser. For all measurements, the same sample was used: a platelet with (±100) faces of a few square millimetres size and a thickness of a few hundreds microns.

In the kinematic diffraction theory, which is usually used for the treatment of resonant diffraction, and in the case of a sample larger than the beam and much thicker than the absorption length of the crystal material, the intensity of the Bragg reflection corresponding to the reciprocal vector $\boldsymbol{H} = hkl$ is given by [40]

$$I(\boldsymbol{H}) \sim \frac{|F(E, \boldsymbol{e}, \boldsymbol{e}', \boldsymbol{H})|^2}{\mu(E, \boldsymbol{e}) + \mu(E, \boldsymbol{e}') \times g} \tag{14}$$

where the linear absorption coefficients, $\mu(E, \boldsymbol{e})$ and $\mu(E, \boldsymbol{e}')$, depend on both energy E and the polarizations $\boldsymbol{e}, \boldsymbol{e}'$ of the beams, g is a geometrical factor defined as $g = \frac{\sin\alpha}{\sin\beta}$, and α and β are the incident and exit angles with respect to the sample surface. In the case of $h00$ reflections and a (100) sample surface, $g = 1$. Equation (14) assumes that the photon polarization is modified only by the scattering process, but not by absorption. Thus, in order to extract $|F(E, \boldsymbol{e}, \boldsymbol{e}', \boldsymbol{H})|^2$ from the RXS measurements, the measured intensity must be corrected for self-absorption, which requires the determination of the energy dependent absorption and an analysis of its anisotropy.

4.1. Study of the absorption spectrum

Fe_3BO_6 has a crystal structure with point group mmm. The resonant absorption is therefore not isotropic. The dipolar component is trichroic (three independent spectra) and the quadrupolar one contains six independent spectra. The mixed dipole–quadrupole component on the other hand vanishes because the point group permits only parity-even absorption events.

Let us consider the azimuthal dependence of the absorption spectra about the [100] direction, with azimuthal reference [001], for any incidence angle θ and any polarization. Though the polarization vector is generally not an eigenstate of the optical system, we can make this approximation if the anisotropy is not too strong compared to the isotropic absorption. Within this approximation, the linear absorption

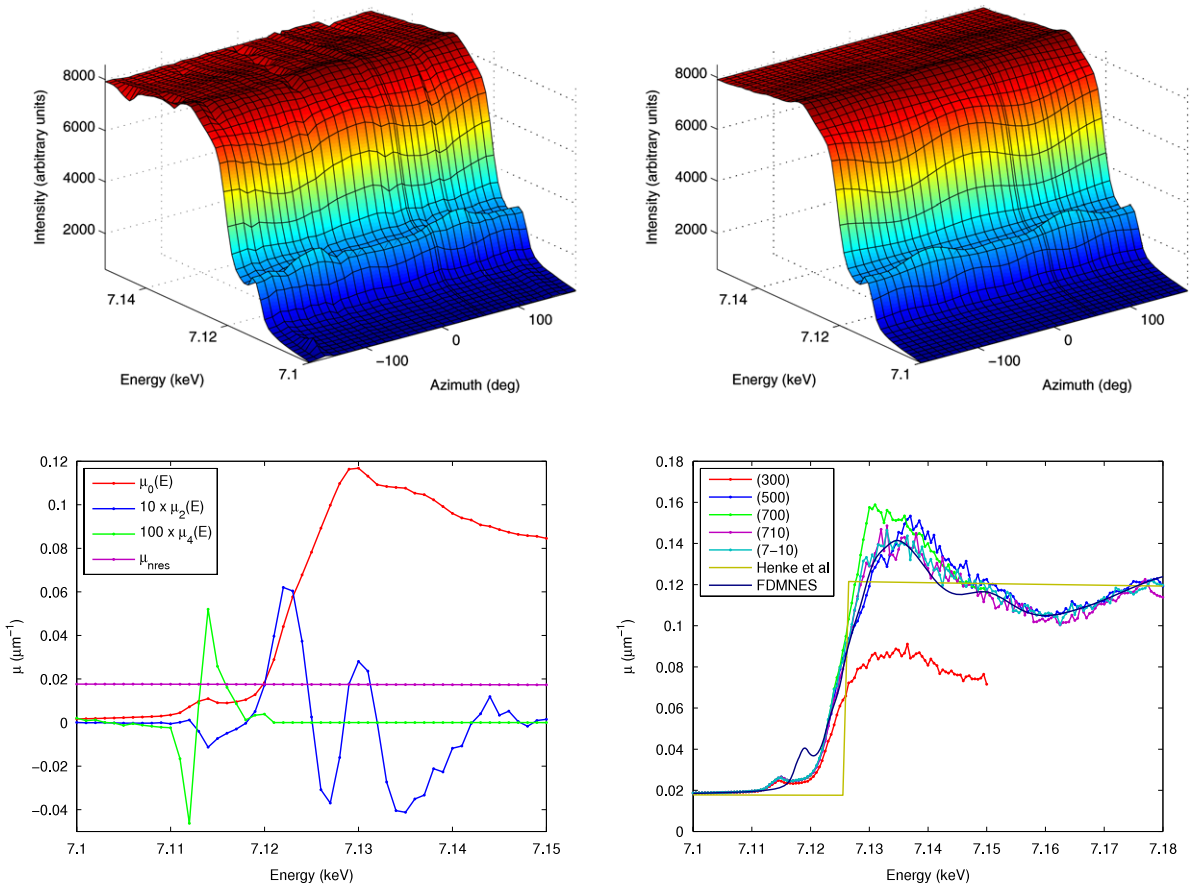

Figure 2. Upper left: energy–azimuth map of the fluorescence of Fe_3BO_6 at the Fe K edge and about the [100] direction. The detector is at 90°, vertical to the incident beam, the incident angle is around 20° and the polarization is horizontal. Upper right: calculated map from the fit. Lower left: fit parameters. Lower right: isotropic part of the absorption spectrum, as obtained from fitting the fluorescence data. The *hkl* indices refer to the RXS reflections at which the fluorescence data were recorded. Except for reflection 300 the mutual agreement of the fitted spectra is reasonably good. The 300 data set was rather poor due to the combination of the low incidence angle, the large beam size and a sample inhomogeneity. Except for the pre-edge region the general shape of the absorption coefficient is in agreement with the FDMNES calculations (see section 5). For comparison, the values calculated from Henke's tables [41] are also shown.

coefficient μ is proportional to the absorption cross-section. According to Brouder's formalism [30], μ can be written as

$$\begin{aligned}\mu(E,\theta,\psi) &= \mu_{\text{nres}} + \mu_{\text{K}}(E,\theta,\psi)\\ &= \mu_{\text{nres}} + \mu_0(E,\theta) + \mu_2(E,\theta)\cos(2\psi)\\ &\quad + \mu_4(E,\theta)\cos(4\psi)\end{aligned} \tag{15}$$

where the non-resonant part of the absorption μ_{nres} is almost constant across the K edge, whereas the resonant part at the K edge, μ_{K}, is different for different eigenpolarizations. Since μ_0 and μ_2 are largely dominated by the dipole contribution they can be considered as independent of θ in the case of σ polarized light. The term μ_4 is of quadrupolar origin and occurs only in the pre-edge region; μ_2 and μ_4 are later referred to as twofold and fourfold parts, respectively.

A full energy–azimuth map of fluorescence was measured from the same sample at the DLS beamline I16, with the detector at 90° from the incident beam, the incident angle at 20° and the polarization perpendicular to the [100] axis: for simplicity, we shall now refer to this polarization as σ, as for the scattering case (figure 2, top left).

For a thick sample, the measured fluorescence intensity is [42]

$$\frac{I_{\text{f}}(E)}{I_0(E)} \propto \frac{\mu_{\text{K}}(E)}{\mu(E) + g\mu(E_{\text{f}})} \tag{16}$$

where the angular dependence is implicit. $E_{\text{f}} = 6.4$ keV is the average energy of the $K_{\alpha 1}$ and $K_{\alpha 2}$ fluorescence lines. The energy–azimuth map was fitted with $\mu_0(E)$, $\mu_2(E)$, $\mu_4(E)$ and a scale factor as free parameters. $\mu_{\text{nres}}(E)$ and $\mu(E_{\text{f}})$ were calculated from the atomic data tables [41]. The final fit parameters and the resulting model map are shown in figure 2. The measured and calculated maps do not show any significative difference, attesting to the good quality of the fit. The twofold and fourfold parts of the absorption are clearly evidenced and are respectively one and two orders of magnitude lower than the isotropic part. Note that these independent spectra are still dependent on θ, and measurements at different incidence angles would be needed to evidence this. However, only the quadrupolar part of the absorption is θ dependent with this polarization, and it is expected to vanish except around the pre-edge feature. $\mu_0(E)$ and $\mu_2(E)$ are therefore a good approximation of the

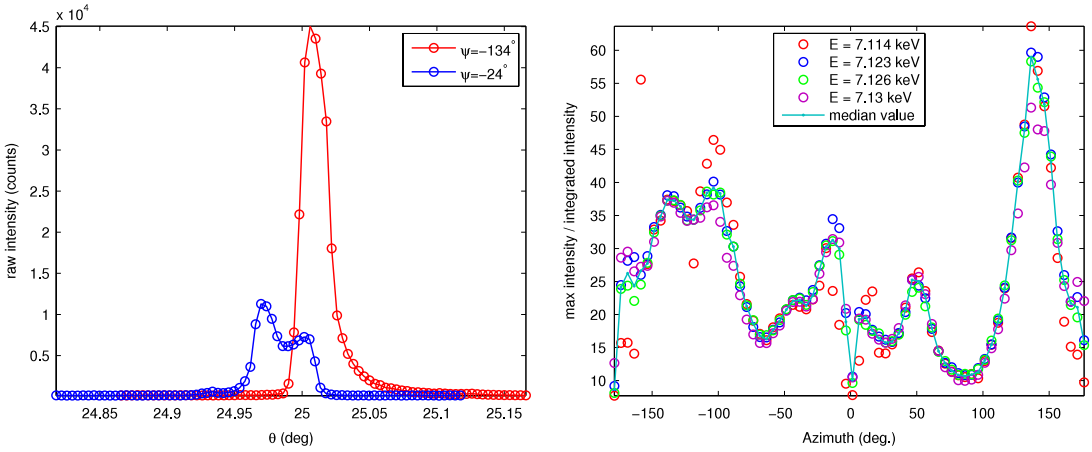

Figure 3. Left: rocking curves of the reflection 500 at two different azimuths, illustrating the variability of the shape (hence the crystal quality). Right: maximum intensity to integrated intensity ratio of the 500 reflection rocking curves versus azimuth. The intensities recorded at four different energies show that this ratio is essentially energy independent.

isotropic and twofold components of the dipole absorption for σ-polarized light.

A similar procedure was applied to the fluorescence data measured along with the RXS data at XMaS: each energy–azimuth map was separately fitted. Since, however, the data sets were rather noisy, the two- and fourfold components could not be extracted. The isotropic curves are shown in figure 2 (bottom right). Although the forbidden reflections change the light polarization from σ to π, as shown in the theoretical section, the diffracted intensity is so small compared to the incident intensity that one can infer in first approximation that the fluorescence results only from absorption events involving σ polarized photons. Thus, the case described in the previous paragraph applies, and the dipolar absorption should be the same for all $h00$ reflections.

4.2. RXS data reduction

For the extraction of $|F(\boldsymbol{H})|^2$ from the measured data several effects must be taken into account.

The first one is the self-absorption effect, which distorts the energy spectra. In principle, the absorption also has an angular dependence, but as shown in section 4.1 ignoring it is not a bad approximation. Hence, an effective absorption spectrum was calculated by averaging the four reasonably isotropic absorption curves derived from the fluorescence measured at the reflections 500, 700, 710 and $7\bar{1}0$ (300 was not considered for the reasons given above). According to equation (14), the measured data were multiplied by $\mu(E, \boldsymbol{e}) + g\mu(E, \boldsymbol{e}') \approx (1+g)(\mu_{\mathrm{nres}} + \mu_0(E))$, where g is 1 for the $h00$ reflections. Of course, correcting the data with an isotropic absorption spectrum and neglecting its azimuthal dependence introduces errors. From figure 2, bottom left panel, we estimate that these can locally amount to 15% (particularly in the pre-edge region), and to 5% at energies above the edge.

Another problem is the inhomogeneity of the sample, which leads to strong variations of the rocking curve profiles obtained in azimuthal scans: the ratio of the maximum height of the rocking curve to its integrated intensity is not constant. Since the energy–azimuth maps were recorded 'on the fly', i.e. without integrating each rocking curve, we had to correct for the azimuthal dependence of the maximum/integrated intensity ratio of rocking curves, that were recorded at a few sample energies (figure 3). As expected, these ratios seem to be energy independent within the small energy range of the spectra.

The last effect to correct for is multiple scattering. In fact, most of the energy spectra are severely contaminated by multiple scattering (figure 4, top left). To correct for this, we eliminated all experimental points whose intensities relative to those of their azimuthal neighbours exceeded a threshold value, which was chosen as the standard deviation of the next-neighbour intensity variation. The eliminated points were then replaced by interpolations from the remaining points. This method takes advantage of the small azimuthal step size (5°) of the experimental data and most of the multiple scattering could be removed, the remaining contributions being too small to have significant impact on subsequent data analysis (figure 4, top right).

The resulting two-dimensional azimuth–energy maps of intensities of the forbidden reflections 300, 500 and 700 are shown in figure 4.

In a further step, according to the theoretical predictions (equations (11)–(13)), the corrected data $I(E, \psi)$ were fitted with the model function:

$$I(E, \psi) = |a(E)\sin\psi + b(E)\mathrm{e}^{\mathrm{i}\Phi(E)}\sin(3\psi)|^2 \qquad (17)$$

where $a(E)$, $b(E)$ and $\Phi(E)$ are real positive parameters (figure 5). The differences between the 'corrected' maps and the fitted maps are essentially due to the residual multiple scattering. As expected, the fit curves show a strong twofold component, mainly due to the dipole–dipole scattering, which largely hides the twofold dipole–quadrupole scattering as well as the twofold part of the quadrupole–quadrupole scattering. The fourfold component of the quadrupole–quadrupole scattering appears only in the pre-edge region, as expected. The small fourfold features at

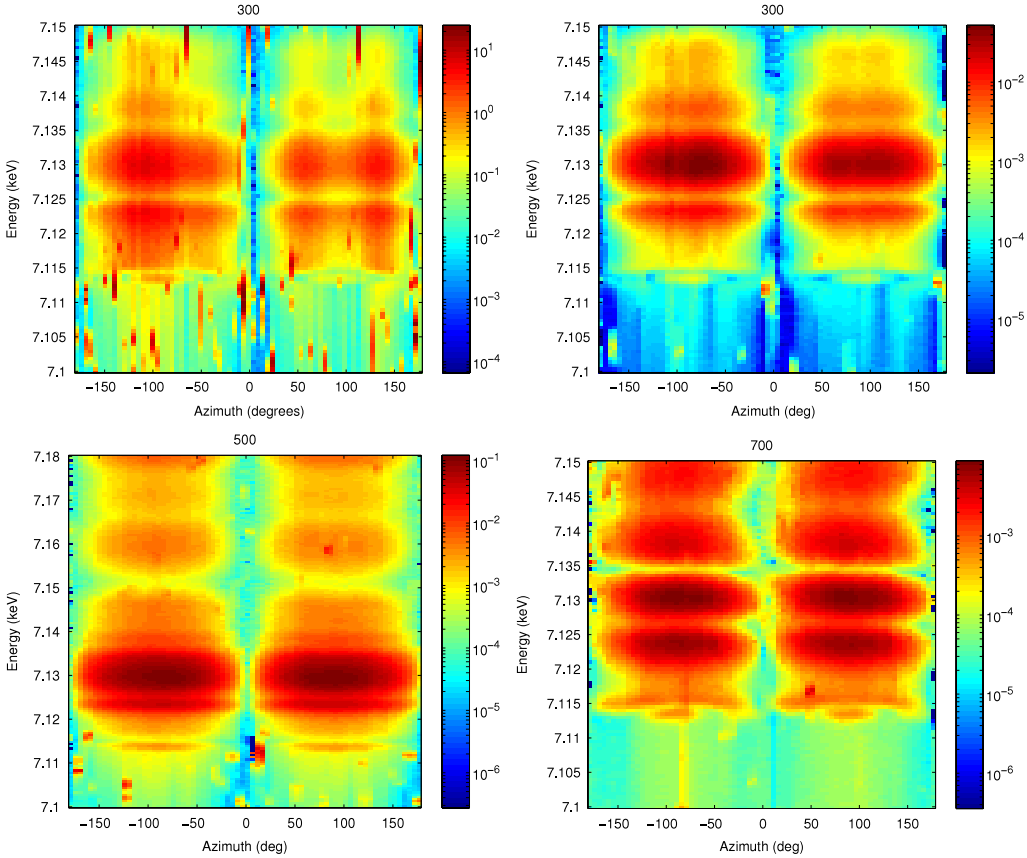

Figure 4. Energy–azimuth maps of the 300 (top), 500 (bottom left) and 700 (bottom right) forbidden reflections. For the 300, both raw data (left) and corrected data (right) are shown. Note the distortion of the azimuthal dependence by the poor crystal quality, the distortion of the energy dependence by the self-absorption, and the dense multiple scattering. For the 500 and 700, only corrected data are shown.

higher energies may be explained by the isotropic absorption correction: the twofold aspects of the scattering ($|\sin\psi|^2$) and of the absorption ($\cos 2\psi$) yield a weak fourfold contribution, like the interference between the $\sin\psi$ and $\sin 3\psi$ terms in the scattering amplitude. This contribution appears on the main peaks of the reflections 300 and 500, where both intensity and absorption are large. Elsewhere it is within the noise of the measurement. Its weakness proves that our approximation of isotropic absorption suffices for the correction of the RXS data. The phase parameter $\Phi(E)$ remains close to $0[\pi]$, except for reflection 700, for which the fourfold feature seems to be shifted in phase by $\pi/2[\pi]$ against the twofold one. However, the data for the fit are too noisy to state this with confidence.

4.3. Thermal-motion-induced scattering and magnetic scattering

So far, our analysis is based on the hypothesis that the forbidden reflections are exclusively due to time-even scattering of the atoms in their nominal positions, i.e. we neglect contributions of thermal motion induced scattering (TMI). TMI is the derivative of the scattering tensor of the atom at rest with respect to its position. Due to the predominating dipole–dipole scattering, its main contribution is therefore a third rank tensor with the same symmetry constraints as those of the symmetric dipole–quadrupole scattering tensor, and, being related to thermal displacements of atoms, TMI almost vanishes at low temperatures. Therefore, we measured the reflection 700 also at low temperature. The energy spectra at room temperature (300 K) and at low temperature (8 K) are almost identical (figure 6, left). This finding proves that TMI must be small compared to the tensor of scattering at rest.

Also so far, we have considered the crystal as non-magnetic although it is weakly ferromagnetic with a paramagnetic transition at $T_c = 508$ K. Despite the small ferromagneticity, most of its ordered moments follow an antiferromagnetic order with propagation vector [000]: the spins form two ferromagnetic sub-layers in the (a, b)-plane, and the coupling between the two sub-layers, along the c-axis, is antiferromagnetic [43]. It undergoes a spin reorientation transition at $T_{SR} = 415$ K, when the antiferromagnetic and ferromagnetic axes swap their directions: the antiferromagnetic axis goes from [001] below T_{SR} to [100] above T_{SR} [44]. As a consequence of the antiferromagnetic component, the magnetic structure factor does not vanish for the forbidden reflections $h00$, $h = 2n + 1$, i.e. both resonant and non-resonant magnetic scattering can contribute to their intensities.

The magnetic moments are carried by the Fe^{3+} cations, which, in iron oxides, are normally in the high spin state

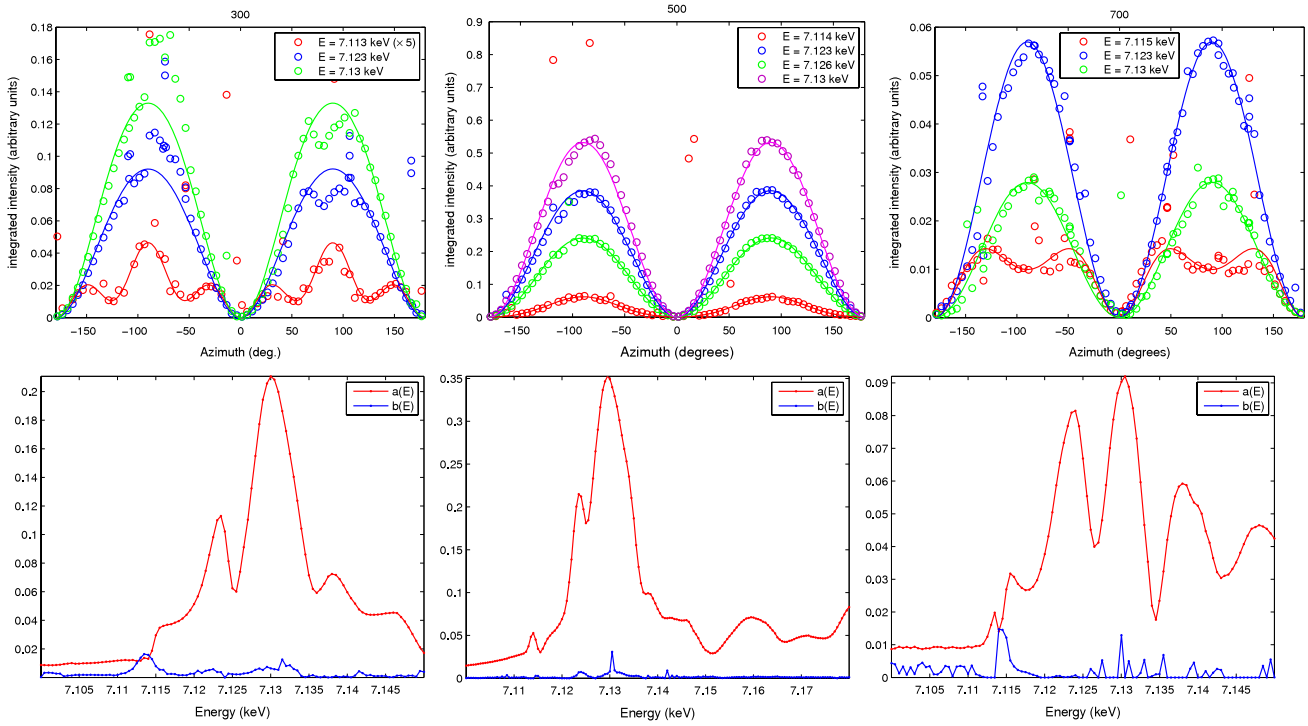

Figure 5. Top: selected azimuthal dependences and their fits against equation (17). A hint of asymmetry, visible in the pre-edge of reflections 300 and 700, can be attributed to non-resonant magnetic scattering. Bottom: fit parameters $a(E)$ and $b(E)$ of the energy–azimuth maps of figure 4 with the model given in equation (17). Left, 300; middle, 500; right, 700.

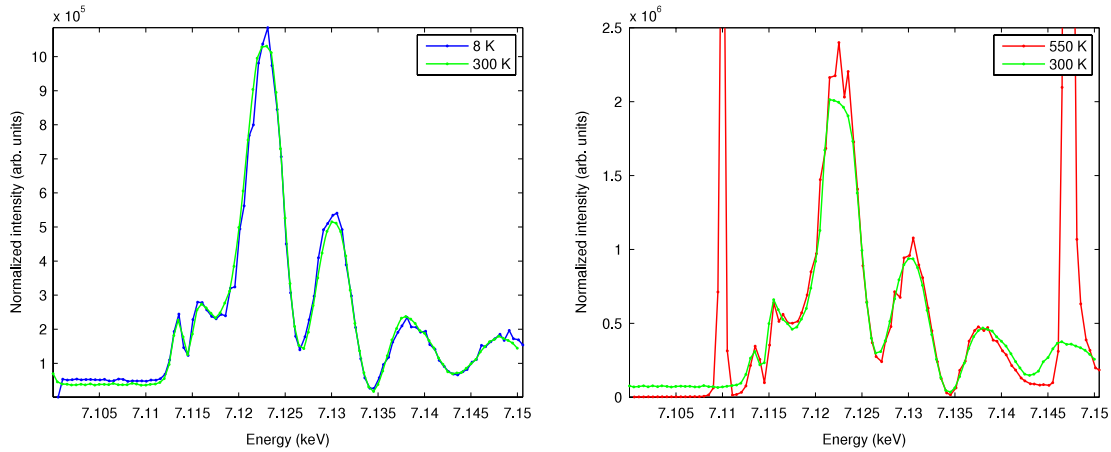

Figure 6. Energy spectra of the forbidden reflection 700 at low temperature (8 K), room temperature (300 K) and elevated temperature (550 K). The normalized intensities without absorption corrections are presented. Note that the data at room temperature were taken at XMaS, whereas the data 8 and 550 K were measured at DLS I16. Left: azimuth $\psi = 90°$. Right: azimuth $\psi = -72° = -90° + 18°$ at 550 K and $\psi = -108° = -90° - 18°$ at 300 K.

($S = 5/2$ and $L = 0$) [45]. Since resonant electric transitions are only sensitive to orbital moments (and to the spin moments via spin–orbit coupling), a resonant magnetic scattering contribution to the forbidden reflections can be expected to be very weak, but a contribution of non-resonant magnetic scattering cannot be ruled out. Indeed, the experimental spectra derived at room temperature and low temperature do not vanish below the absorption edge, which suggests measurable effects of non-resonant magnetic scattering (figures 5 and 6). This assumption of non-resonant magnetic scattering is confirmed by the measurements performed at 550 K, i.e. well above the paramagnetic transition, which failed to yield any measurable signals below the edge (figure 6, right). Close to and above the edge, the strong absorption reduces the scattering volume in such a way that non-resonant contributions become small compared to the resonance enhanced contributions. Since our aim is to observe and demonstrate the interferences of the RXS from the two iron sites, we will not further focus on the non-resonant region and ignore magnetic scattering in the ensuing data analysis.

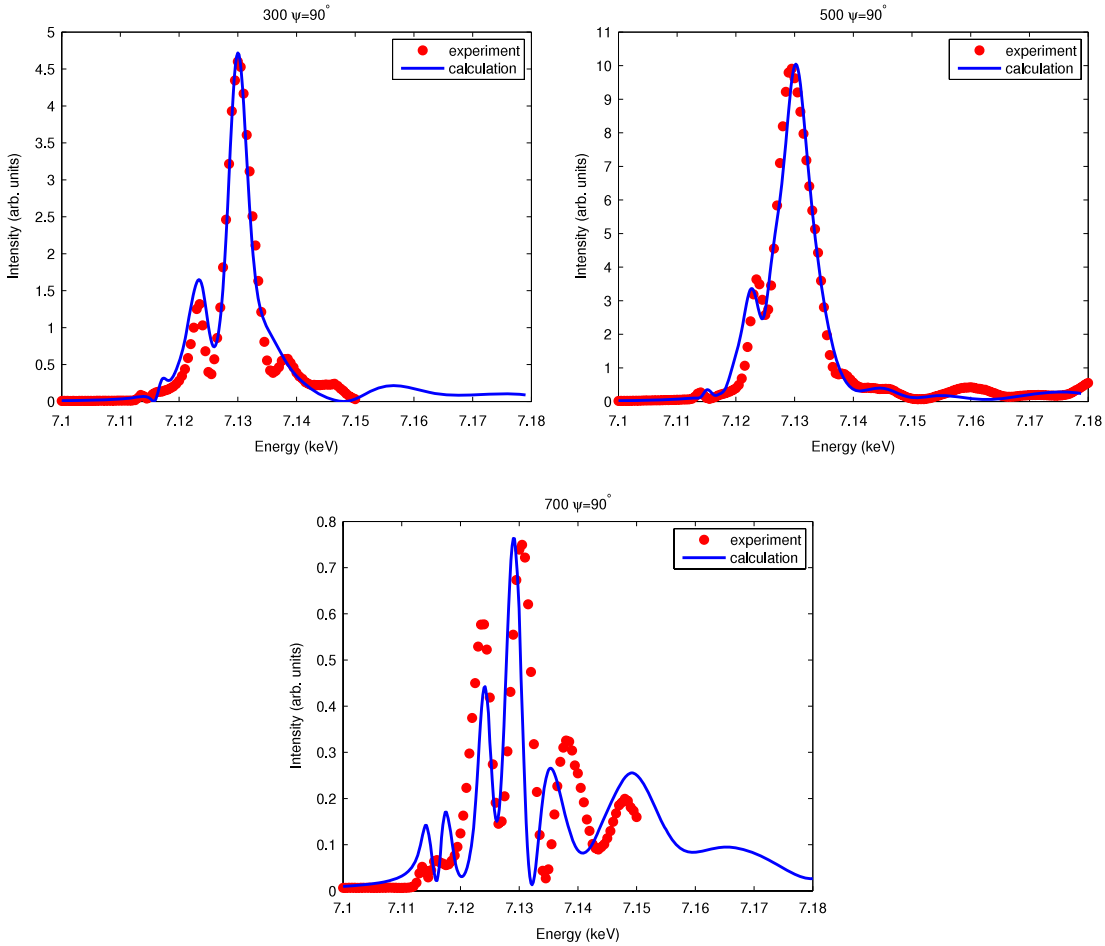

Figure 7. Energy spectra of the reflections 300, 500 and 700 at the azimuth $\psi = 90°$: FDMNES calculations versus experimental data.

5. Fitting the energy and azimuthal dependences

Our symmetry analysis has shown that the structure factors of the $h00, h = 2n + 1$, reflections can be conveniently described by 12 tensor components (six for each site), but azimuthal scans allow only for extracting two independent spectra per reflection. Therefore, the experimental results can only be interpreted by numerical simulations. To this purpose, the FDMNES code [46] was used for calculating the absorption cross-sections and the structure factors $|F(\boldsymbol{H})|^2$ of the forbidden reflections. This information served to yield data that can be compared with the experimental intensities, after correction. Using the multiple scattering option of the code, with the Hedin–Lundquist potential, it was attempted to optimize the model parameters with respect to best agreements with the experimental values of $I(\boldsymbol{H})$ and $\mu(E)$.

Let us refer to the strong reflections above 7.120 keV as main peaks and to the weak peaks below 7.120 keV as pre-edge peaks. The numerical simulation of the various contributions to the tensor atomic factors show that, while the main peaks are mainly due to the dipole–dipole contributions from both of the iron cations, the pre-edge peaks can be described by higher order terms producing complex azimuthal and energy structures. Despite the dipole–dipole origin of the main peaks, their intensity modelling is not simple, just because of the interference of the radiation scattered at the two Fe positions. It follows from table 1 that 4(c) and 8(d) structure factors interfere in very different ways for the 300, 500 and 700 reflections. Indeed, the experimentally observed 300 and 500 reflections are strong, in contrast to the weak 700, and the 700 energy spectrum looks rather different from those of 300 and 500 (figures 4, 5 and 7).

In the course of simulations, the main peaks of the three measured reflection intensities were fitted first. Neglecting higher order terms in their energy range, the model intensities depend on two parameters only: $D_{xz}^{8(\mathrm{d})}$ and $D_{xz}^{4(\mathrm{c})}$. Table 1 shows that the dipole–dipole component of the 300 intensity is mainly provided by the 8(d) sites, while the contribution of the 4(c) sites is very small. This circumstance allows for a convenient extraction of $D_{xz}^{8(d)}$, whereupon $D_{xz}^{4(\mathrm{c})}$ could be extracted from the 500 spectrum, once $D_{xz}^{8(\mathrm{d})}$ was known. Finally, the 700, in which the radiation interference between the iron sites is mainly destructive, was used for fine tuning, because the destructive interference makes modelling extremely sensitive to the ratio of both parameters. A satisfactory description of the 700 spectrum could only be achieved upon introducing an energy shift of 0.7 eV between both contributions. This chemical shift can be rationalized by the different environments of the iron cations occupying two inequivalent sites. Then, it was checked that the same set of parameters allows for reasonably good 'fits' of all three reflections (figure 7) as well as of the absorption (figure 2).

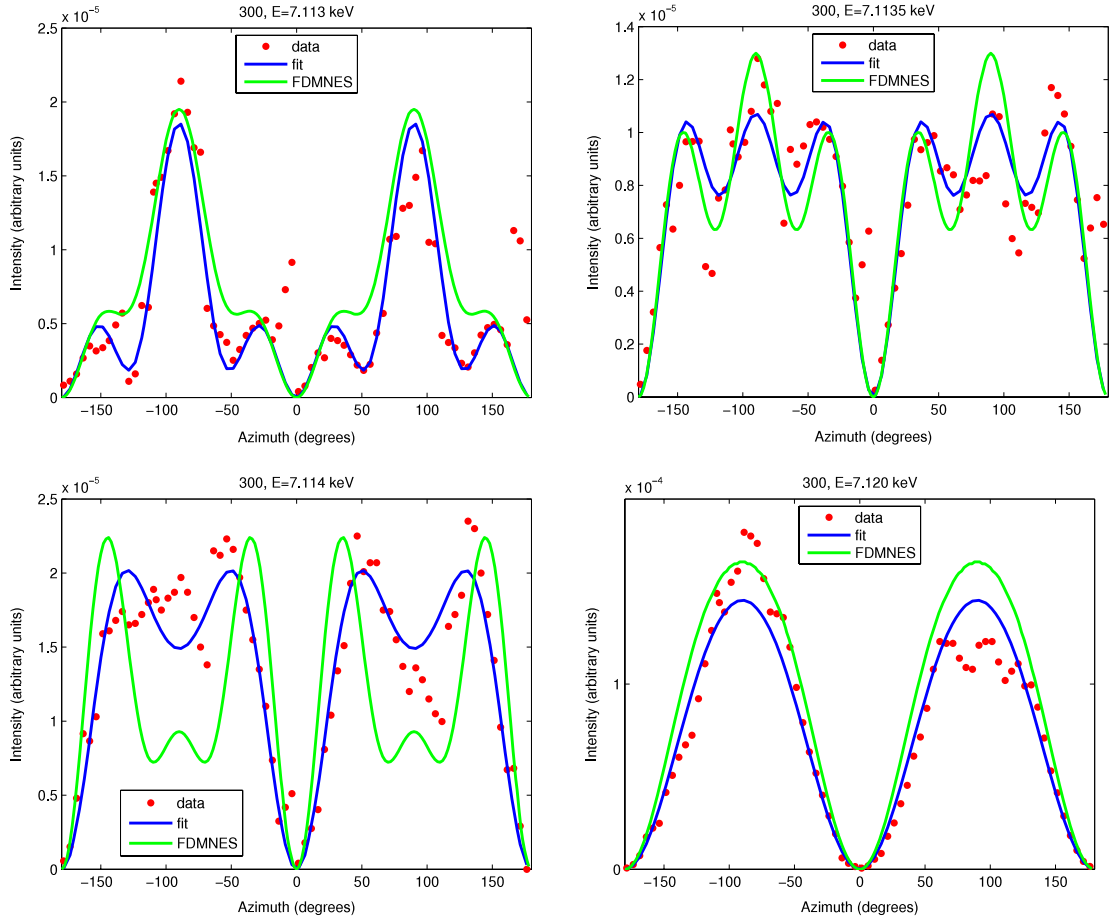

Figure 8. Azimuthal dependence of the reflection 300 at 7.113, 7.1135, 7.114 and 7.12 keV. Comparison between experimental data ('data'), fit against equation (17) ('fit'), and simulation with FDMNES ('FDMNES'). The simulation fulfils equation (17), but the coefficients are not the best fit to the data.

The key step of the simulation procedure is the convolution that describes the spectral broadening $\Gamma(E)$, due to the core- and valence-electron lifetimes in the excited state. This function being unknown, FDMNES supposes $\Gamma(E)$ to grow smoothly, e.g. like

$$\Gamma = \Gamma_{\text{hole}} + \Gamma_m \left[\frac{1}{2} + \frac{1}{\pi} \arctan\left(\frac{\pi}{3} \frac{\Gamma_m}{E_{\text{large}}} \left(e - \frac{1}{e^2} \right) \right) \right] \quad (18)$$

where $e = \frac{E - E_{\text{Fermi}}}{E_{\text{cent}}}$. The five parameters Γ_{hole}, Γ_m, E_{cent}, E_{Fermi}, and E_{large}, that provided the smallest differences from the experimental data, were obtained with the optimization procedure of the FDMNES code, yielding $E_{\text{Fermi}} = -6.5$ eV, $\Gamma_m = 24$ eV, $E_{\text{cent}} = 14$ eV, $E_{\text{large}} = 10$ eV, $\Gamma_{\text{hole}} = 2$ eV.

Since the main peaks, near and above the edge, result from the dipole–dipole scattering, their intensities observed upon rotation about the scattering vector display a stable twofold azimuthal dependence. In the pre-edge region, however, the features observed result from the interplay between the dipole–quadrupole and quadrupole–quadrupole terms so that more complex azimuthal dependences are displayed, which, in addition, vary strongly with energy (figure 8). Their intensity values are too small to allow for detailed modelling, but the FDMNES calculations using the previously determined convolution parameters reproduce the general shape of the data reasonably well (figure 8).

Figure 9 shows the calculated dipole–quadrupole and quadrupole–quadrupole contributions to reflection 300 of each iron position, at 7.114 and 7.115 keV. Although these energies seem very close to each other, the various contributions show strong energy dependent changes of azimuthal behaviour, which affect the total intensity.

6. Conclusions

Resonant x-ray diffraction near the iron K edge was studied in iron orthoborate, both theoretically and experimentally. The complex energy and azimuthal dependences of the 300, 500 and 700 forbidden reflection intensities are explained as resulting from the interference between the radiation scattered from the two crystallographically inequivalent iron positions: 8(d) and 4(c). In the dipole–dipole approximation, the 300 intensity results mainly from Fe at the 8(d) position, whereas the 500 and 700 intensities result respectively from constructive and destructive interferences of radiation scattered from Fe at both crystallographic positions. The features in the pre-edge region can be explained by the interplay of dipole–quadrupole and quadrupole–quadrupole processes.

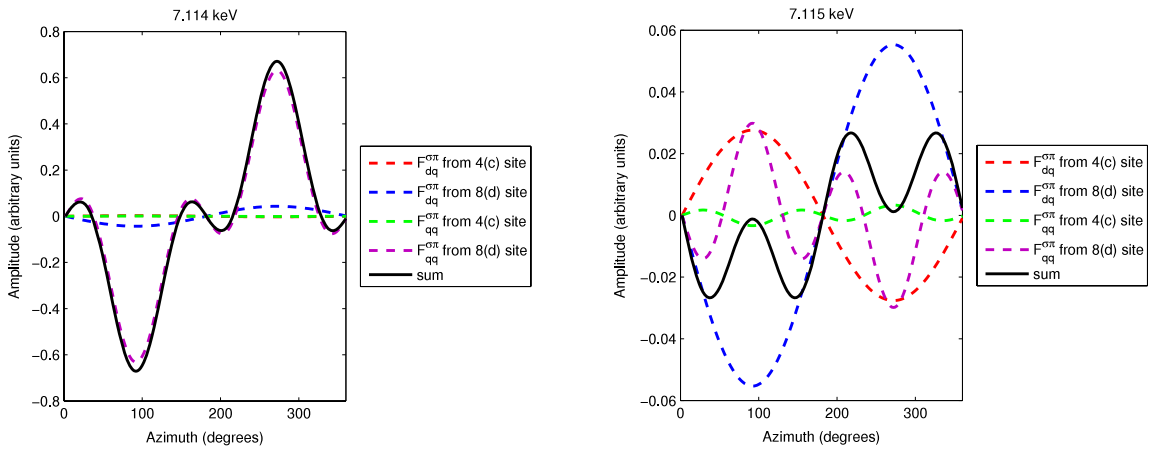

Figure 9. Azimuthal dependences of the dipole–quadrupole and quadrupole–quadrupole contributions to the 300 reflection at 7.114 keV (left) and 7.115 keV (right). The FDMNES convolution parameters are the same as previously determined.

Due to the low point symmetry of the iron sites, the large number of parameters required for the full description of the resonant scattering prevented their complete determination. Nevertheless, the dipole–dipole components could be extracted from the large part of the energy spectra where higher rank processes are comparatively weak, i.e. near and above the K edge. Theoretical calculations with the FDMNES code and subsequent fits of the experimental spectra suggest an energy difference of 0.7 eV between the K edges of the two non-equivalent iron atoms. This chemical shift is attributed to the different crystallographic environments, to which RXS is very sensitive. The measurements of the 700 reflection, whose net intensity and energy spectrum were found to be stable over a wide temperature range, indicate the absence of significant contributions of magnetic and/or thermal-motion-induced scattering.

The investigations demonstrate also the remarkable sensitivity of RXS to the interplay of various radiation contributions, and simultaneously that a thorough analysis is possible despite its apparent non-triviality. However, only studies of both energy and azimuthal dependences of several forbidden reflection intensities provide the possibility to distinguish contributions from different crystallographic sites and hence to study differences in the electronic interactions of atoms thereon. Finally, it should be noted that excellent experimental data could be extracted from measurements that were seriously affected by the poor crystal quality, frequent multiple scattering and strong self-absorption. This finding demonstrates, as in earlier studies, e.g. [47], that RXS as a local probe is restricted neither to using nearly perfect crystals nor to especially favourable diffraction geometries.

Acknowledgments

The authors acknowledge the support of the XMaS staff for the RXS measurements. This work was supported by grants RFBR 07-02-00324 and INTAS 01-0822.

References

[1] Hodeau J-L, Favre-Nikolin V, Bos S, Renevier H, Lorenzo E and Berar J-F 2001 *Chem. Rev.* **101** 1843–67
[2] Lovesey S W, Balcar E, Knight K S and Fernandez-Rodrigues J 2005 *Phys. Rep.* **411** 233–89
[3] Dmitrienko V E, Ishida K, Kirfel A and Ovchinnikova E N 2005 *Acta Crystallogr.* A **61** 481–93
[4] Collins S P, Lovsey S W and Balcar E 2007 *J. Phys.: Condens. Matter* **19** 213201
[5] Templeton D H and Templeton L K 1985 *Acta Crystallogr.* A **41** 365
[6] Dmitrienko V E 1983 *Acta Crystallogr.* A **39** 29
[7] Dmitrienko V E 1984 *Acta Crystallogr.* A **40** 89
[8] Templeton D H and Templeton L K 1994 *Phys. Rev.* B **49** 14850
[9] Dmitrienko V E and Ovchinnikova E N 2001 *Acta Crystallogr.* A **57** 642–8
[10] Di Matteo S, Joly Y, Bombardi A, Paolasini L, de Bergevin F and Natoli C 2003 *Phys. Rev. Lett.* **91** 257402
[11] Finkelstein K D, Shen Q and Shastri S 1992 *Phys. Rev. Lett.* **69** 1612
[12] Carra P and Thole T 1994 *Rev. Mod. Phys.* **66** 1509
[13] Gibbs D, Moncton D E and D'Amico K L 1985 *J. Appl. Phys.* **57** 3619
[14] Hannon J P, Trammell G T, Blume M and Gibbs D 1988 *Phys. Rev. Lett.* **61** 1245
[15] Namikawa K, Ando M, Nakajima T and Kawata H 1985 *J. Phys. Soc. Japan* **54** 4099–102
[16] Ovchinnikova E N and Dmitrienko V E 2000 *Acta Crystallogr.* A **56** 2–10
[17] Ji S, Song S, Koo J, Lee K-B, Park Y J, Kim J Y, Park J-H, Shin H J, Phyee J S, Oh B H and Cho B K 2003 *Phys. Rev. Lett.* **91** 257205
[18] Dmitrienko V E, Ovchinnikova E N and Ishida K 1999 *JETP Lett.* **99** 938–42
[19] Dmitrienko V E and Ovchinnikova E N 2000 *Acta Crystallogr.* A **56** 340–7
[20] Kokubun J, Kanazava M, Ishida K and Dmitrienko V E 2001 *Phys. Rev.* B **64** 073203
[21] Kirfel A, Grybos J and Dmitrienko V E 2002 *Phys. Rev.* B **66** 165202
[22] Detlefs C 2004 *Physica* B **345** 45–8
[23] Collins S P, Laundy D, Dmitrienko V E, Mannix D and Thompson P 2003 *Phys. Rev.* B **68** 064110
[24] Beutier G, Collins S P, Ovchinnikova E N and Dmitrienko V E 2009 in preparation

[25] Kokubun J, Watanabe A, Uehara M, Ninomiya Y, Sawai H, Momozawa N, Ishida K and Dmitrienko V E 2008 *Phys. Rev.* B **78** 115112
[26] Garcia J, Subias G, Proietti M G, Renevier H, Joly Y, Hodeau J L, Blasco J, Sanchez M C and Berar J C 2000 *Phys. Rev. Lett.* **85** 578–81
[27] Kolchinskaya A M, Artem'ev A N, Dmitrienko V E, Zabelin F V, Maevski A G, Ovchinnikova E N, Oreshko A P, Sarkisyan V A and Joly Y 2006 *Kristallografiya* **51** 222
Kolchinskaya A M, Artem'ev A N, Dmitrienko V E, Zabelin F V, Maevski A G, Ovchinnikova E N, Oreshko A P, Sarkisyan V A and Joly Y 2006 *Crystallogr. Rep.* **51** 192 (Engl. Transl.)
[28] Blume M 1994 *Magnetic Effects in Anomalous Dispersion//in Resonant Anomalous X-Ray Scattering* ed G Materlik, C J Sparks and K Fisher (Amsterdam: Elsevier)
[29] Belyakov V A and Dmitrienko V E 1989 *Sov Phys.—Usp.* **18** 267–99
[30] Brouder C 1990 *J. Phys.: Condens. Matter* **2** 701–38
[31] Lovesey S W and Collins S P 1996 *X-Ray Scattering and Absorption by Magnetic Materials* (Oxford: Clarendon)
[32] Sirotine Yu and Shaskolskaia M P 1982 *Fundamentals of Crystal Physics* (Moscow: Mir)
[33] Stone A J 1975 Properties of Cartesian-spherical transformation coefficients *J. Phys. A: Math. Gen.* **9** 485
[34] White J G, Miller A and Nielsen R E 1965 *Acta Crystallogr.* **19** 1060
[35] Kovalenko P P, Labushkin V G, Ovsepyan A K, Sarkisov E R and Smirnov E V 1984 *Pis. Zh. Eksp. Teor. Fiz.* **39** 471
Kovalenko P P, Labushkin V G, Ovsepyan A K, Sarkisov E R and Smirnov E V 1984 *JETP Lett.* **39** 573 (Engl. Transl.)
[36] Tolpekin I G, Kovalenko P P, Labushkin V G, Ovchinnikova E N, Sarkisov E R and Smirnov E V 1988 *JETP* **94** 329–43
[37] Bayukov O A, Buznik V M, Ikonnikov V P, Petrov M I and Popov M A 1976 *Fiz. Tverd. Tela* **18** 2435
Bayukov O A, Buznik V M, Ikonnikov V P, Petrov M I and Popov M A 1976 *Sov. Phys.—Solid State* **18** 1421 (Engl. Transl.)
[38] Kovalenko P P, Labushkin V G, Ovsepyan A K, Sarkisov E R, Smirnov E V, Prokopov A R and Seleznev V N 1984 *Fiz. Tverd. Tela* **26** 3068
Kovalenko P P, Labushkin V G, Ovsepyan A K, Sarkisov E R, Smirnov E V, Prokopov A R and Seleznev V N 1984 *Sov. Phys.—Solid State* **26** 1849 (Engl. Transl.)
[39] Diehl R and Brandt G 1975 *Acta Crystallogr.* B **31** 1662
[40] James R W 1950 *The Optical Principles of the Diffraction of X-Rays* (London: Bell and Sons)
[41] Henke B L, Gullikson E M and Davis J C 1993 X-ray interactions: photoabsorption, scattering, transmission, and reflection at $e = 50$–30000 eV, $z = 1$–92 *At. Data Nucl. Data Tables* **54** 181
[42] Pfalzer P, Urbach J-P, Klemm M, Horn S, denBoer Marten L, Frenkel Anatoly I and Kirkland J P 1999 *Phys. Rev.* B **60** 9335
[43] Mal'tsev V I, Naiden E P, Zhilyakov S M, Smolin R P and Borisyuk L M 1975 *Kristallografiya* **21** 113–7
[44] Wolfe R, Pierce R D, Eibschutz M and Nielsen J W 1969 *Solid State Commun.* **7** 949–52
[45] Cornell R M and Schwertmann U 2003 *The Iron Oxides* (Weinheim: Wiley–VCH)
[46] www.neel.cnrs.fr/fdmnes
[47] Kirfel A, Petcov A and Eichhorn K 1991 *Acta Crystallogr.* A **47** 180–95